

Modeling photoacoustic spectral features of micron-sized particles

This content has been downloaded from IOPscience. Please scroll down to see the full text.

2014 Phys. Med. Biol. 59 5795

(<http://iopscience.iop.org/0031-9155/59/19/5795>)

View [the table of contents for this issue](#), or go to the [journal homepage](#) for more

Download details:

IP Address: 141.117.24.130

This content was downloaded on 29/09/2014 at 03:05

Please note that [terms and conditions apply](#).

Modeling photoacoustic spectral features of micron-sized particles

Eric M Strohm¹, Ivan Gorelikov², Naomi Matsuura³ and Michael C Kolios¹

¹ Department of Physics, Ryerson University, Toronto, Canada

² Physical Sciences, Sunnybrook Research Institute, Toronto, Canada

³ Department of Medical Imaging, University of Toronto, Toronto, Canada

E-mail: mkolios@ryerson.ca

Received 23 April 2014, revised 29 July 2014

Accepted for publication 1 August 2014


Published 10 September 2014

Abstract

The photoacoustic signal generated from particles when irradiated by light is determined by attributes of the particle such as the size, speed of sound, morphology and the optical absorption coefficient. Unique features such as periodically varying minima and maxima are observed throughout the photoacoustic signal power spectrum, where the periodicity depends on these physical attributes. The frequency content of the photoacoustic signals can be used to obtain the physical attributes of unknown particles by comparison to analytical solutions of homogeneous symmetric geometric structures, such as spheres. However, analytical solutions do not exist for irregularly shaped particles, inhomogeneous particles or particles near structures. A finite element model (FEM) was used to simulate photoacoustic wave propagation from four different particle configurations: a homogeneous particle suspended in water, a homogeneous particle on a reflecting boundary, an inhomogeneous particle with an absorbing shell and non-absorbing core, and an irregularly shaped particle such as a red blood cell. Biocompatible perfluorocarbon droplets, 3–5 μm in diameter containing optically absorbing nanoparticles were used as the representative ideal particles, as they are spherical, homogeneous, optically translucent, and have known physical properties. The photoacoustic spectrum of micron-sized single droplets in suspension and on a reflecting boundary were measured over the frequency range of 100–500 MHz and compared directly to analytical models and the FEM. Good agreement between the analytical model, FEM and measured values were observed for a droplet in suspension, where the spectral minima agreed to within a 3.3 MHz standard deviation. For a droplet on a reflecting boundary, spectral features were correctly reproduced using the FEM but not the analytical model. The photoacoustic spectra from other common particle configurations such as

particle with an absorbing shell and a biconcave-shaped red blood cell were also investigated, where unique features in the power spectrum could be used to identify them.

Keywords: photoacoustics, finite element method, spectral analysis

 Online supplementary data available from stacks.iop.org/PMB/59/5795/mmedia

(Some figures may appear in colour only in the online journal)

1. Introduction

The photoacoustic effect is the emission of a pressure wave from a structure after irradiation by an energy source, typically a laser. For spatial scales of interest in biomedical photoacoustic imaging, a portion of the frequency of the emitted wave is in the ultrasonic range. This wave is called a photoacoustic or optoacoustic wave due to the laser-induced method in which it was generated (Wang 2009). Photoacoustic imaging requires an optical absorbing structure in the medium for a wave to be generated. Most tissues have negligible optical absorption throughout the visible and infrared spectrum where photoacoustic imaging is commonly used. The main absorbing structure in tissue is the blood, and the main chromophore in the red blood cells (RBCs) is haemoglobin. This endogenous source of contrast has been exploited *in vivo* for the detection of tumours (Zhang *et al* 2006), photoacoustic tomography (Wang and Hu 2012), functional imaging of the brain (Wang *et al* 2003, Nasiriavanaki *et al* 2013, Tsytarev *et al* 2013), and imaging the vasculature (Kolkman *et al* 2003, Beard 2011). In addition, exogenous photoacoustic contrast agents with high contrast properties have been used to help identify breast, prostate and brain tumors (Manohar *et al* 2007, Agarwal *et al* 2007, Kim *et al* 2009, Yao *et al* 2013).

Recently, perfluorocarbon (PFC) emulsions loaded with absorbing nanoparticle (NPs) have gained popularity as theranostic agents (Strohm *et al* 2010, 2011, Wilson *et al* 2012). The optical absorbing nanoparticles are a necessary component for the generation of photoacoustic signals, as PFC liquids have negligible absorption in the visible and near-infrared wavelengths. When irradiated with sufficient optical energy, the NP-loaded micron-sized droplets emit photoacoustic signals. These contrast agents have unique signal signatures compared to endogenous photoacoustic sources in tissue, and these signatures can be used to localize and quantify the amount of agent present. Since this photoacoustic signal signature is more readily differentiated in the frequency domain, a model that can rapidly and accurately represent the frequency content of the signal is important for agent optimization and detection.

When a particle absorbs energy, it undergoes a rapid thermoelastic expansion that results in the emission of a photoacoustic wave in the ultrasonic frequency range. Neglecting viscosity and thermal conduction, the photoacoustic waves generated due to absorption of optical energy H (such as a laser) is the solution to the inhomogeneous wave equation

$$\frac{1}{c^2} \frac{\partial^2 p}{\partial t^2} - \nabla^2 p = \frac{\beta}{C_p} \frac{\partial H}{\partial t} \quad (1)$$

where p is the pressure, t is time, c is the sound speed, β is the thermal expansion coefficient, and C_p is the heat capacity (Morse and Ingard 1968). Analytical solutions for the generation of photoacoustic waves have been derived for simple geometries just as spheres (Diebold *et al* 1990). Assuming the pressure wave and energy source vary with time as $\exp(-i\omega t)$, the

solution to equation (1) for the photoacoustic waves generated from a liquid homogenous spherically symmetric particle is

$$P(f) = i \left(\frac{\mu_a I_0 c_p \beta}{4\pi C_p (r/a)} \right) \frac{(\sin q - q \cos q)/q^2}{(1 - \frac{\rho_p}{\rho_f})(\sin q/q) - \cos q + i \frac{c_p \rho_p}{c_f \rho_f} \sin q} \quad (2)$$

where f is the frequency, a is the particle radius, μ_a is the optical absorption coefficient, I_0 is the incident laser intensity, ρ is the density, the subscripts p and f refer to the particle and fluid, respectively, and $q = 2\pi fa/c_p$ (Diebold and Westervelt 1988). Good agreement has been found between analytical solutions and measured photoacoustic signals for liquid homogeneous spheres (Diebold *et al* 1990). However, the analytical solution breaks down for complex configurations such as multi-particle systems, particles near boundaries, or particles that have a heterogeneous composition. In these cases, the photoacoustic signal must be numerically simulated. Several tools exist for calculating the photoacoustic signal; the k-wave toolbox calculates the time domain signal using coupled first order acoustic equations (Treeby and Cox 2010); Field II simulates the ultrasound field using linear systems theory (Jensen and Svendsen 1992, Jensen 1996); and COMSOL Multiphysics (Comsol, USA) uses a finite element model (FEM) to simulate the photoacoustic signal propagation in either the time or frequency domain.

In a FEM, the system is divided into smaller components which can then be iteratively solved. Recently, photoacoustic FEMs have examined temperature and displacement effects in tissue (Xu 2004, Xu *et al* 2006), photoacoustic tomography reconstruction (Yuan and Jiang 2007, Yao and Jiang 2009) and photoacoustic propagation in tissue (Wang *et al* 2012). A FEM was used to investigate the photoacoustic spectral content of photoacoustic waves generated in cases where the analytical solution cannot be used. The model takes into account wave generation and propagation immediately after the particles are irradiated and absorb the laser energy, and assumes that the particle instantly and uniformly absorbs the laser energy resulting in a pressure increase relative to the surrounding non-absorbing areas. The FEM then solves for the propagation of the acoustic waves due to the pressure differential within the system using the wave equation

$$\frac{1}{c^2} \frac{\partial^2 p}{\partial t^2} - \nabla^2 p = 0. \quad (3)$$

The FEM solution was solved for four different geometries (figure 1): 1) a particle in suspension, 2) a particle on a highly reflecting boundary, 3) a non-homogeneous particle with an absorbing shell and non-absorbing core, and 4) an irregularly shaped particle. For a particle in suspension (scenario 1), the pressure waves simply radiate outwards and attenuate within the surrounding medium. For a particle near a boundary (scenario 2), waves emitted from the droplet will be reflected by the boundary back into the droplet. Scenario 3 simulates a particle with an inhomogeneous composition, a thin shell of optical absorbing material surrounding a non-absorbing liquid core. This simulates contrast agents where the optical absorbing material is contained in the shell instead of the core (Lovell *et al* 2011, Huynh *et al* 2012, Sun *et al* 2013). Scenario 4 simulates an irregularly shaped particle, for example a RBC with a bi-concave shape. Scenarios 1 and 2 were compared to experimental photoacoustic measurements of micron-sized PFC particle containing NPs as optical absorbers, while scenarios 3 and 4 demonstrate how the FEM could be used where analytical solutions do not exist.

This study shows that the photoacoustic power spectrum can be used to extract information about the particle that cannot be obtained using time domain methods alone. Using the FEM, matching solutions to the analytical equation were found for ideal cases such as a particle in

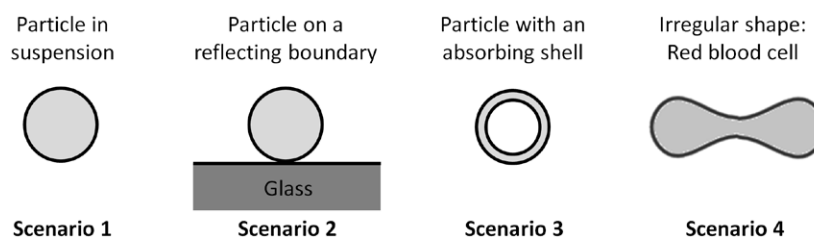


Figure 1. Particles and geometries examined in this study. The grey-shaded region indicates the optically absorbing area. Four scenarios were investigated: (a) a spherical homogeneous particle in suspension, (b) a homogeneous particle on a hard reflecting boundary such as glass, (c) a particle with an absorbing shell and non-absorbing core, and (d) an irregularly shaped particle such as a red blood cell.

suspension. In the case where the analytical model cannot be used, the FEM correctly predicts the extra spectral features as measured from particles on a boundary. The FEM can be applied for even more complex systems, providing insight into how the frequency content of the photoacoustic waves is modified as a function of the particle/boundary characteristics.

2. Method

2.1. Perfluorocarbon droplets

Lead sulphide (PbS) nanoparticles were synthesized, coated with silica (Yi *et al* 2005, Gorelikov and Matsuura 2008), then fluorinated for miscibilization into PFP (Synquest, USA) (Matsuura *et al* 2009, Gorelikov *et al* 2011). PbS-loaded PFP droplets were prepared using 5 mL deionized water, 0.15 mL PFP solution containing PbS nanoparticles, and 0.03 mL anionic fluorosurfactant (Zonyl FSP, Sigma-Aldrich, USA) using emulsification with 10 μm pore polymer membranes (Whatman, USA), following coarse emulsification by vortexing. The droplet diameters were measured using a microscope with an optical scale.

2.2. Photoacoustic measurements

A SASAM photoacoustic microscope (Kibero GmbH, Germany) was used for all measurements and is described in detail in reference (Strohm *et al* 2011). Briefly, a 1064 nm laser was focused by a 10 \times objective (0.30 numerical aperture) onto the sample from below, and a 375 MHz transducer (60° aperture, 42% bandwidth) positioned above the sample recorded the photoacoustic signals generated by the sample. The laser was operated at a 2 kHz pulse repetition frequency with a 700 ps pulse width. This pulse width was less than the stress and thermal confinement times of a 1 μm diameter liquid PFC droplet, calculated to be 2 ns and 8 μs , respectively. The signals were amplified by 40 dB (Miteq, USA) and digitized at 8 GS s^{-1} (0.125 samples ns^{-1}). All measurements were made at 36 °C. The droplet diameter was found by comparing the recorded image to a calibrated scale using the 10 \times objective. The error associated with this optical measurement is $\pm 0.5 \mu\text{m}$ when using a 10 \times objective, primarily due to the small particle sizes examined.

The photoacoustic signals from particles in suspension and on a boundary were investigated using micron-sized nanoparticle-loaded droplets (figure 2). In scenario #1, a droplet deposited on top of an agar gel surrounded by water was used to approximate a droplet in suspension. The agar gel has similar properties as water (Zell *et al* 2007) and minimized any

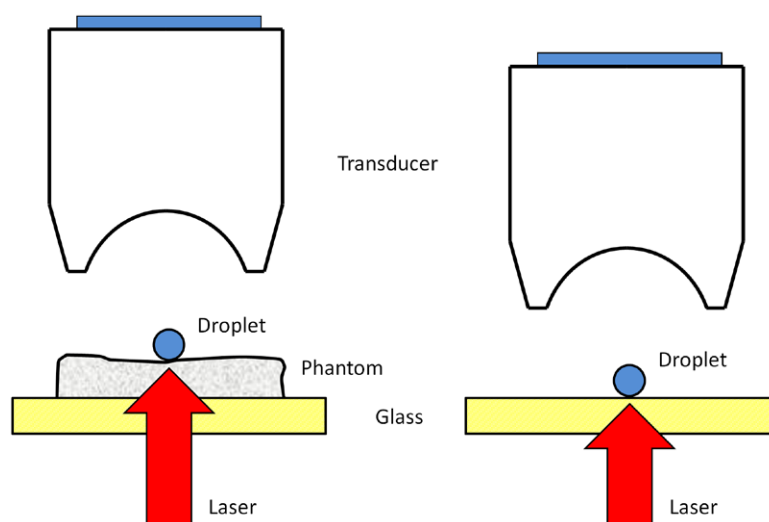


Figure 2. Diagram showing the two droplet configurations measured. The transducer positioned above the droplet recorded the photoacoustic signals from the droplet when irradiated by a 1064 nm laser from below. The photoacoustic signals from a droplet with a soft boundary (droplet on an agar surface, left) and a highly reflecting boundary (droplet directly on a glass substrate, right) were measured.

reflections that might occur. In scenario #2, the droplet was deposited directly on the glass substrate, a highly reflecting surface for ultrasound. All measurements averaged 100 RF-lines to increase the signal to noise ratio (SNR). The transducer response was removed from the signal by normalizing the signal as described in (Baddour *et al* 2005), then a Hamming window and 100–500 MHz bandpass filter were applied. These processed signals were then compared to the analytical model and FEM solution.

2.3. The finite element model

Finite element models for each scenario were solved using the COMSOL Multiphysics (COMSOL, USA) software package. A transient acoustics 2D axisymmetric model was used to calculate the photoacoustic emission from particles using the wave equation (equation (1)). For this calculation, the particle diameter must be known, but the error associated with optical imaging for particles $<5\ \mu\text{m}$ in diameter is $\pm 0.5\ \mu\text{m}$. Since the exact diameter could not be accurately measured, simulations were completed with a range of diameters similar to the measured diameter. The simulation with the most similar photoacoustic spectrum compared to the experimental results was used. In the model, the initial pressure was set to unity inside the particle, and zero elsewhere. For scenario 3, a particle with an absorbing polymer shell was simulated where the pressure within the shell of thickness 250 nm was set to unity, and zero elsewhere including the droplet core. The shell was composed of Poly-lactide-coglycolic acid (PLGA), which has a known density ($1340\ \text{kg m}^{-3}$) and sound speed ($2300\ \text{m s}^{-1}$) (Parker *et al* 2010). The model assumed the laser energy was absorbed instantaneously (infinitesimally narrow laser pulse) so that the pressure wave did not propagate prior to the start of the simulation. The mesh within the particle was set to $0.01\ \mu\text{m}$, and $0.05\ \mu\text{m}$ outside. An absorbing boundary condition was set at a $10\ \mu\text{m}$ radius, the outer boundary of the simulation. The photoacoustic signal directly above the particle

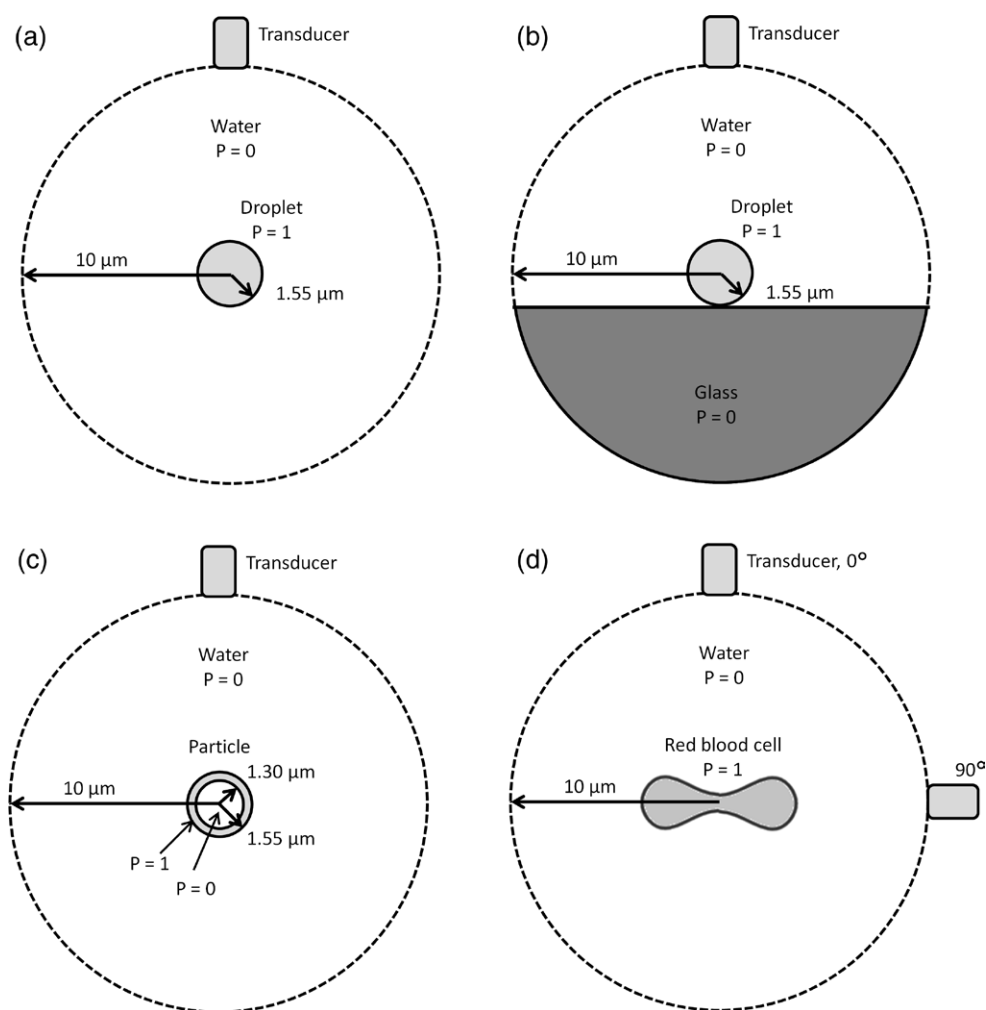


Figure 3. The COMSOL model geometries used in this study. (a) A 3.1 μm droplet in a water suspension, (b) a droplet on glass (diameters ranged from 2.8–3.6 μm), (c) a 3.1 μm particle in a water suspension but with an optically absorbing 250 nm PLGA shell surrounding a non-absorbing PFC core and (d) a red blood cell with a 7.8 μm diameter. In (a), (b) and (d), the pressure inside the particle was set to unity, and for the surround water the pressure was set to zero. In (c), the pressure of the shell was set to unity, and the core was set to zero. The signal was recorded directly above the droplet.

was recorded as a function of time with a 0.125 ns step size (the same as the experimental acquisition rate). Diagrams of the four modeling scenarios are depicted in figure 3. The FEM simulated a propagation time of 80 ns, which took approximately 3–5 h for 800 000 degrees of freedom using a computational cluster containing six dual-core Opteron nodes and 40 GB of memory. The parameters used in the model are listed in table 1, including the diameter measured optically and the final diameter determined by a comparison between measured and simulated photoacoustic signals. Measurements from four droplet sizes were used in this study to compare to the theoretical models: one droplet in suspension, and three droplets on a glass substrate.

The speed of sound is a required parameter in the simulations. The boiling point of bulk PFP is 29 °C, and experiments were performed at 36 °C. The PFP liquid inside the droplets exists in a superheated state where the boiling point is increased by 40–50 °C compared to the bulk phase (Kripfgans *et al* 2000); therefore it is difficult to measure the properties of bulk liquid PFP at temperatures greater than 29 °C. Studies measured the sound speed of PFP to be 468 m s⁻¹ using 2 MHz at 22 °C (Jongsma 1979) and 477 m s⁻¹ using 1 MHz at 25 °C (Narayana and Swamy 1989). Measurements of several PFC liquids other than PFP showed a linear decrease in sound speed with increasing temperature from 25–36 °C at 10 MHz (Marsh *et al* 2002). The change in sound speed was -2.778 m s⁻¹ °C⁻¹ for FC-72, the liquid with the closest molecular weight and structure to PFP. Assuming the change in sound speed with temperature of PFP is similar to the FC-72 even when in a superheated state, the sound speeds of 468 m s⁻¹ (22 °C) and 477 m s⁻¹ (25 °C) would be 429 m s⁻¹ and 446 m s⁻¹ at 36 °C, respectively. Averaging these values gives 438 m s⁻¹, which was used in the FEM and analytical simulations. Sound dispersion was neglected as it was found that PFC liquids have only a 1.5% increase from 100–1000 MHz (Strohm and Kolios 2011) and considered negligible over the frequency range used in this study.

The properties of the red blood cell were different than the droplets. The size and shape were calculated using an equation derived empirically (Evans and Fung 1972). The RBC geometry is shown in figure 3(d). The sound speed used in the model was 1650 m s⁻¹ (similar to other sound speeds measured (Dukhin *et al* 2006, Mohamed *et al* 2012)) and the density was 1100 kg m⁻³ (Godin *et al* 2007, Grover *et al* 2011). The blood cell interior was assumed to be homogeneous throughout, both optically and acoustically.

3. Results

3.1. Finite element model validation

The FEM solutions of two PFP droplets (3.1 μm and 5.0 μm) suspended in water were calculated using COMSOL with the parameters described in table 1. The photoacoustic signal was calculated as a function of time at a point on the outer system boundary over an 80 ns time length. The FEM solution was compared to the analytical solution (equation (2)) using identical parameters. The signals were normalized to maximum amplitude, and no other signal processing methods or filters were applied. Good agreement in both the time and frequency domains were observed as shown in figure 4, thus validating the FEM methodology.

3.2. Particles in suspension and on a glass boundary

The simulated time domain and power spectrum for a 3.1 μm droplet in suspension and on a glass substrate using the analytical solution (equation (2)) and the results are shown in figure 5. The parameters used for modeling the droplet in each case were identical. Both scenarios show spectral minima around 200, 345, 490 and 635 MHz, however, the spectrum from the droplet on glass has additional spectral minima located around 275, 405 and 540 MHz.

The measured time domain signal for a 3.1 μm droplet on agar (simulating a droplet in suspension) and a 3.1 μm droplet on the glass substrate are shown in figures 6(a) and (b), respectively. These signals appear different than the simulations in figure 5 as they are band-limited due to the limited transducer response. Despite similar droplet sizes, the signal from the droplet on a glass boundary exhibits additional signal information. This is a result of the pressure wave rebounding from the glass substrate back towards to transducer, which can alter the frequency content of the photoacoustic signal.

Table 1. Modeling parameters used in the finite element method models.

Parameter	Particle #1	Particle #2	Particle #3	Particle #4	Particle #5	Particle #6
Simulation type	Particle in suspension	Particle on a substrate	Particle on a substrate	Particle on a substrate	Shelled Particle in suspension	Red blood cell in suspension
Substrate	None	Glass	Glass	Glass	None	None
Optical diameter (μm)	3.4	3.1	4.0	4.2	–	–
Particle diameter (μm)	3.1	2.8	3.1	3.6	3.1	7.8*
Outer boundary (μm)	20	20	20	20	20	20
Particle mesh (μm)	0.01	0.01	0.01	0.01	0.01	0.01
Coupling fluid mesh (μm)	0.05	0.05	0.05	0.05	0.05	0.05
Particle sound speed (m s^{-1})	438	438	438	438	438 (core) 2300 (shell)	1650
Particle density (kg m^{-3})	1620	1620	1620	1620	1620 (core) 1340 (shell)	1100

*The red blood cell was modeled as a bi-concave shape, with a $7.8\mu\text{m}$ diameter and a height that ranged from $1.0\mu\text{m}$ (at the center) to $2.0\mu\text{m}$ (near the edge).

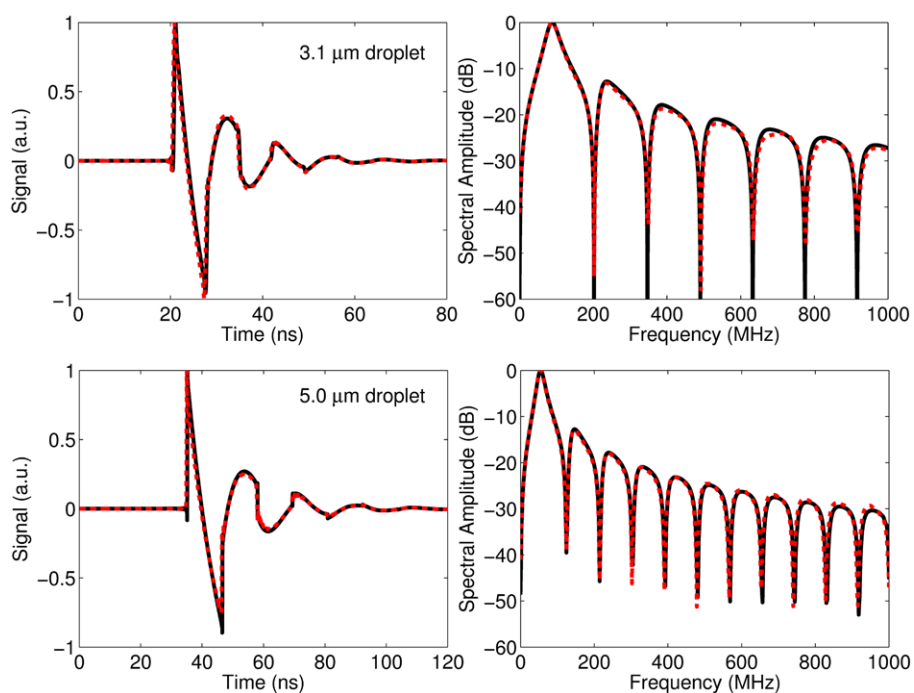


Figure 4. Theoretical waveform and spectrum $3.1\mu\text{m}$ droplet (top) and a $5.0\mu\text{m}$ droplet (bottom) suspended in water obtained from the analytical solution (equation (2), solid black line) and the FEM solution (dotted red line). The signals were normalized to the maximum signal amplitude for comparison. The good agreement in both the time and frequency domains validate FEM methodology.

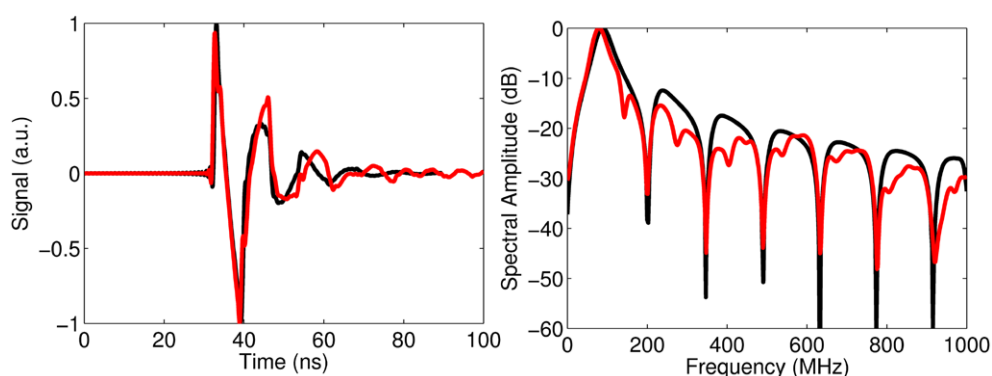


Figure 5. A comparison of the FEM solution of a $3.1\ \mu\text{m}$ droplet on glass (red) and the analytical solution of the same droplet in suspension (black). The signals were normalized to the maximum signal amplitude for comparison. Small changes in the time domain signal result in extra spectral minima for the droplet on a substrate.

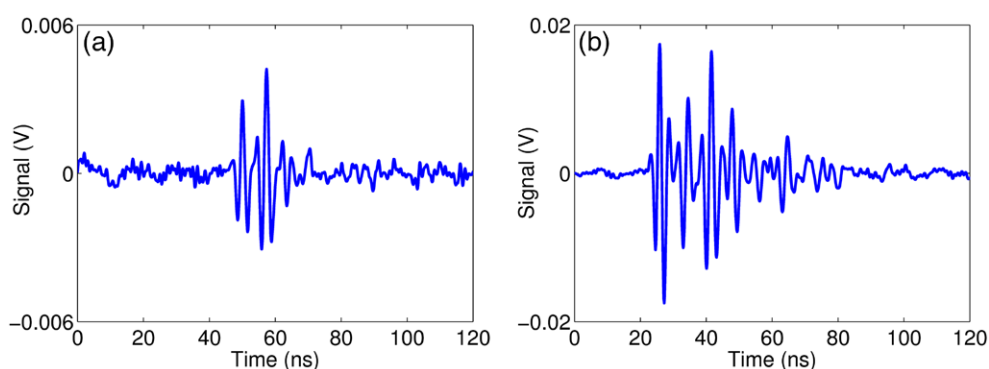


Figure 6. A representative measured photoacoustic signal from (a) $3.1\ \mu\text{m}$ droplet in suspension, and (b) a different $3.1\ \mu\text{m}$ droplet on a glass substrate.

The corresponding power spectra of the two $3.1\ \mu\text{m}$ droplets, along with three other droplets of different diameters measured on a glass substrate, are shown in figure 7. In figure 7(a) (droplet in suspension) the frequencies of the spectral minima at 203, 347 and 492 MHz of the FEM and analytical solution are in good agreement with the measured signal from the droplet (spectral minima located at 205, 348 and 481 MHz). For droplets on glass, the FEM correctly predicts the additional spectral minima that are absent in the analytical solution. Table 2 lists the frequencies of the spectral minima from the measured signal as well as from the analytical and FEM solutions. In all cases, the average standard deviation between the FEM and measured values were less than 8 MHz.

3.3. Irregular particles

The FEM can be applied towards other particle configurations, such as a particle with heterogeneous absorption (particle with an absorbing shell, scenario 3) and an irregularly shaped particle (a red blood cell, scenario 4).

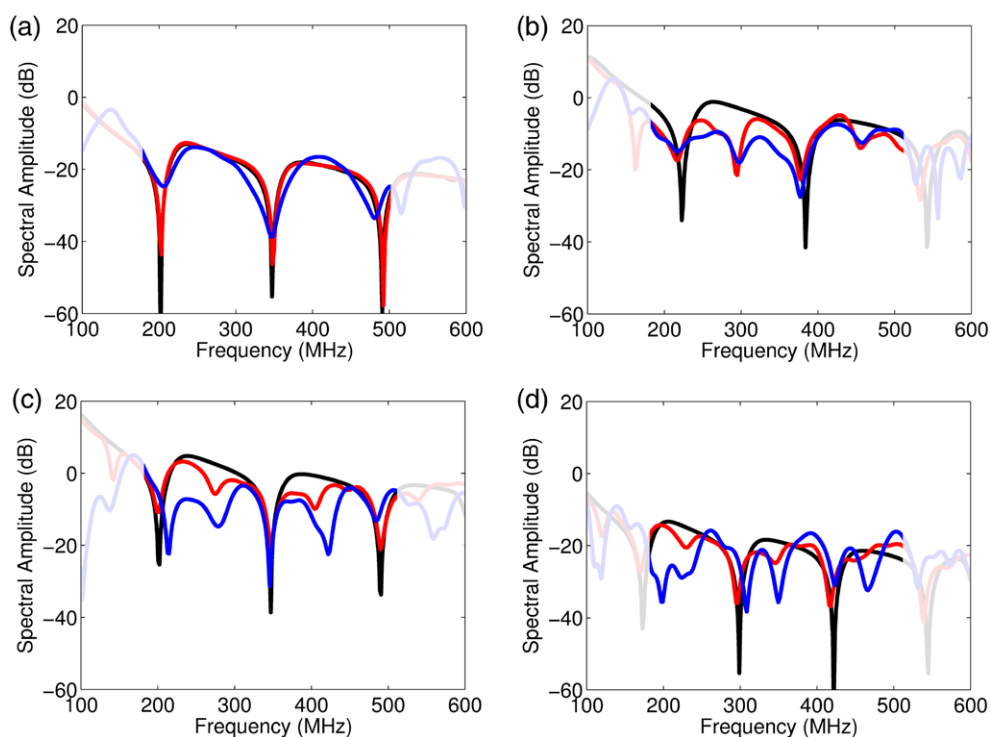


Figure 7. The photoacoustic spectrum from (a) a $3.1\ \mu\text{m}$ droplet on an agar surface (b–d) a droplet on glass with diameters 2.8 , 3.1 and $3.6\ \mu\text{m}$ in diameter, respectively. The measured signals are blue, the analytical solution is black and the FEM solution is red. Good agreement in the location of the experimental and FEM spectral minima were observed for the droplet on an agar surface. For the droplet on a glass substrate, good agreement in the location of the spectral minima were observed between measured and the FEM solution only. The shaded spectral region outside the transducer $-12\ \text{dB}$ bandwidth of approximately $190\text{--}540\ \text{MHz}$ can be considered noise.

Table 2. Spectral minima frequencies of the four droplets in figure 7. The spectral minima associated with the glass substrate are not observed using the analytical model are italicized. The last column is the average standard deviation between the frequency minima of the FEM and measured spectrum.

Droplet	Analytical model (MHz)	FEM (MHz)	Measured (MHz)	Standard deviation
1	203, 347, 492	203, 347, 492	205, 348, 481	3.3 MHz
2	218, 385, 544	219, 295, 377, 457, 533	217, 295, 379, 457, 527	1.4 MHz
3	202, 347, 491	201, 277, 346, 406, 490	215, 279, 346, 422, 484	6.1 MHz
4	173, 299, 422	170, 230, 297, 347, 416	197, 228, 309, 350, 426	7.6 MHz

The FEM was applied to a particle with an optical absorbing shell surrounding a non-absorbing liquid core as shown in figure 3(c). No analytical solution exists for this configuration. Contrast agents with this configuration are under development for use as ultrasound and photoacoustic contrast agents and for cancer therapy, such as polymer-based particles (Kohl *et al* 2011, Sun *et al* 2013, Wang *et al* 2014), liposomes (Volodkin *et al* 2009), porphyrinsomes (Lovell *et al* 2011) and microbubbles (Huynh *et al* 2012). In the FEM, the pressure in the

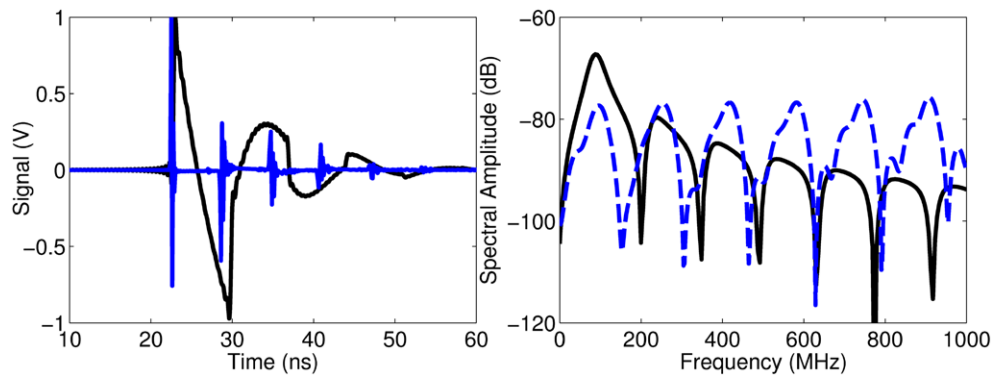


Figure 8. The theoretical photoacoustic time domain signal (left) and power spectrum (right) from a $3.1\ \mu\text{m}$ particle with an optically absorbing PLGA shell 250 nm thick surrounding a non-absorbing liquid core (dotted blue line), compared to the analytical solution of a homogeneously absorbing liquid sphere (solid black line) of the same outer diameter.

shell was set to unity, with the core and surrounding fluid pressure set to zero. All other parameters were the same as scenario 1 (see table 1). The location of the spectra minima and maxima shifted compared to the analytical solution that assumes a homogeneous uniformly absorbing sphere (figure 8). The distance between the spectral minima increased slightly with increasing frequency (from 152 MHz between minima at 200 MHz–164 MHz between minima at 600 MHz), while the distance between the minima was constant for the analytical solution of the uniformly absorbing sphere. The shift in the location of the spectral peaks may be sufficient to differentiate an absorbing particle versus an absorbing shell, however, it is unlikely the shell thickness could be estimated using this procedure.

Red blood cells are shaped like a bi-concave disk with an average diameter of $7.8\ \mu\text{m}$ and a height of $1\text{--}2\ \mu\text{m}$ (Wintrobe *et al* 2009). These irregularly shaped particles cannot be modeled using analytical methods, and are typically approximated as spheres or ellipsoids (Ahuja and Hendee 1977, Saha and Kolios 2011). The FEM is well suited for modeling the photoacoustic signals generated from red blood cells. All parameters were the same as scenario 1 except the shape, density and sound speed (see table 1). The signals were calculated as a function of angle, with a horizontally aligned blood cell (angle of 0° , with the transducer above the cell as depicted in figure 3(d)), and a vertically aligned blood cell (angle of 90° , with the transducer to the right of the cell as depicted in figure 3(d)).

The spectral features shift as a function of measured angle as shown in figure 9. At 0° , minima occur at approximately 200, 450, 750 and 950 MHz. As the blood cell rotates, the spectral minima and maxima shift to higher frequencies. A horizontally oriented blood cell has only one minimum at 800 MHz (Strohm *et al* 2013a, 2013b). The spectra nearly overlap in the 0–100 MHz frequency range. This indicates that the signal is similar regardless of the blood cell orientation, and suggests that the cells can accurately be modeled as a sphere or ellipsoid for computational efficiency within this limited frequency range. However when using frequencies greater than 100 MHz, the blood cell should be modeled as a bi-concave shape as the spectrum depends on the orientation (Strohm *et al* 2013b).

3.4. Visualization of the propagating signal

Animations generated from the FEM simulation show the pressure wave expansion from particles in the four scenarios: a $3.1\ \mu\text{m}$ droplet in suspension, a $3.1\ \mu\text{m}$ droplet on a glass

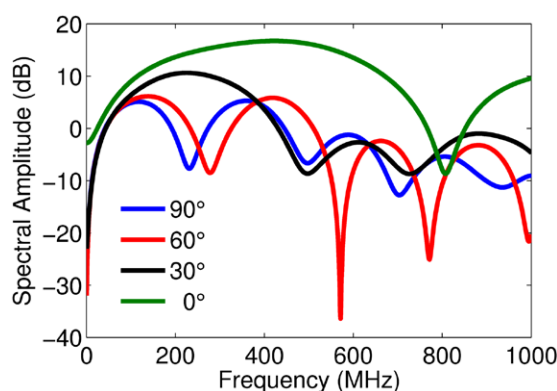


Figure 9. The theoretical photoacoustic spectrum from a single $7.8\mu\text{m}$ diameter red blood cell as a function of angle relative to the receiving transducer from 1–1000 MHz.

substrate, a $3.1\mu\text{m}$ particle in suspension with a shell, and a $7.8\mu\text{m}$ single red blood cell (see supplementary data stacks.iop.org/PMB/59/5795/mmedia). These videos enable visualization of the acoustic wave propagation from the different particles. In all scenarios, a positive pressure wave (red) is shown propagating away from the particle surface, with a negative pressure wave (blue) traveling toward the center. The negative pressure wave then travels outward away from the droplet. This is responsible for the characteristic ‘N’ shape typically observed in photoacoustic measurements of spherical objects, which is analogous to the pressure distribution observed during a bursting balloon (Deihl 1968). For the droplet on the glass substrate, the acoustic wave travels faster through the glass than the coupling fluid, due to the difference in sound speed (5600m s^{-1} in glass compared to 1520m s^{-1} in water). In the case of the absorbing shell (scenario 3), a narrow positive pressure acoustic wave is observed travelling away from the droplet, with a narrow negative pressure wave following a short time after. The wave propagation within the red blood cell is asymmetric due to its irregular shape, and the wave within the cell travels faster than in the other particles as the sound speed in the cell is three times larger than the sound speed in the droplet.

4. Discussion

The nanoparticle-loaded PFC droplets are ideal for photoacoustic measurements. The droplet can be considered homogeneous despite the presence of nanoparticles throughout. The number of nanoparticles in each droplet is calculated to be in the thousands, however the nanoparticles are small and occupy a negligible volume in comparison to the overall droplet volume (Strohm *et al* 2012). The nanoparticles are well dispersed within the volume, and thus upon irradiation, all nanoparticles absorb the energy uniformly and instantaneously. The end result is a photoacoustic wave with characteristics that depend on the droplet composition, not the nanoparticles. We have shown in previous work good agreement between experiment and theory for a nanoparticle loaded droplet in suspension (Strohm *et al* 2012).

Small changes in the photoacoustic time domain signal may not be sufficient to extract information about the particle. We have shown that micron-sized particles have unique spectral features over the wide ultrasound bandwidth used (100–500 MHz). These spectral features can be used to extract the particle parameters, such as their size and sound speed which can then be used for particle identification (Strohm *et al* 2012) or diagnosis of blood-related disease (Strohm *et al* 2013b). This is difficult using the time domain signal alone.

Analytical solutions describing the time and frequency domain photoacoustic signals exist for spherical homogeneous particles, but not for irregularly particles, particles near boundaries or inhomogeneous particles. This study shows that spectral features calculated using the FEM simulation are in good agreement with the analytical model for simple geometries such as a homogenous droplet in suspension, and gives accurate solutions where the analytical model breaks down, such as a droplet positioned on a reflecting boundary. For droplets on glass, the substrate reflects the pressure waves back through the droplet which are then recorded by the transducer. These additional waves result in additional spectral minima not observed from droplets in suspension. Figure 6 shows that the time domain signals for a droplet in suspension and on a reflecting boundary are visually different, but it is not possible to determine the particle parameters or boundary conditions using these signals alone. The corresponding power spectrum in figure 7 shows unique features that help identify these unknowns. Table 2 summarizes the frequency of the spectral minima for all droplets, where the average standard deviation of the frequency of the spectral minima between the FEM and measured was less than 8 MHz.

Our primary interest was the frequency content of the photoacoustic waves, however analytical solutions exist only for simple homogeneous geometries. The FEM could be applied to various scenarios where the analytical solution cannot be used, such as the generation of photoacoustic waves from multiple sources, heterogeneous absorbance and from asymmetric shapes such as the bi-concave shape of red blood cells where the photoacoustic spectral features are known to depend on RBC morphology (Strohm *et al* 2013b).

The amplitude parameters in equation (2) can be adjusted to optimize the photoacoustic signal generation from the droplets to a limited extent. Increasing the laser intensity I_0 is not necessarily feasible as there are limits on the intensities that can be used. The sound speed, thermal expansion coefficient and heat capacity are inherent to the PFC liquid used with small variation between PFC liquids. The easiest way to increase the photoacoustic signal is to increase the absorption coefficient inside the droplet (by increasing the number of nanoparticles or their absorption coefficient), or to increase the droplet size. This would increase the total absorption coefficient of the droplet, ultimately increasing the signal amplitude. Moreover, for theranostics, larger droplets will offer opportunities to carry a larger therapeutic payload for activated release by light directly at a tumor site. These high frequencies cannot be used *in vivo* due to high attenuation of ultrasound, but could be used to identify cells and/or particles in samples using the photoacoustic spectrum. Understanding how the photoacoustic signal is generated by these particles and propagates in a medium assists in development and optimization of these particles for eventual use *in vivo* using clinical ultrasound and photoacoustic instruments.

5. Conclusion

The photoacoustic power spectrum can be used to extract information about a particle that cannot be obtained from the time domain signal alone. Analytical solutions can be used to calculate the photoacoustic signal from simple geometries such as spheres, but cannot be used for irregularly-shaped particles or particles near boundaries. In those cases, a finite element method can be used to calculate the particle-dependent spectral features. The FEM can easily be adapted to other configurations such as multi-particle systems, and particles with heterogeneous absorption properties and/or boundary conditions where analytical solutions cannot be used. This study establishes that particle types can be identified according to unique spectral features in the photoacoustic spectrum.

Acknowledgements

E Strohm was supported through a Natural Sciences and Engineering Research Council of Canada (NSERC) doctoral scholarship. J Carl Kumaradas (Ryerson University) is acknowledged for his assistance in using the Ryerson computational cluster. This research was undertaken, in part, thanks to funding from NSERC and the Canada Research Chairs Program awarded to M Kolios. Funding to purchase the equipment was provided by the Canada Foundation for Innovation, the Ontario Ministry of Research and Innovation, and Ryerson University. This study was supported, in part, by the Ontario Research Fund-Research for Excellence Program, by the Cancer Imaging Network of Ontario (CINO) supported by Cancer Care Ontario with funds from the Ministry of Health and Long-Term Care, and by Prostate Cancer Canada, proudly funded by the Movember Foundation – Grant # D2014-7.

References

- Agarwal A, Huang S W, O'Donnell M, Day K C, Day M, Kotov N and Ashkenazi S 2007 Targeted gold nanorod contrast agent for prostate cancer detection by photoacoustic imaging *J. Appl. Phys.* **102** 064701
- Ahuja A S and Hendee W R 1977 Effects of red cell shape and orientation on propagation of sound in blood *Med. Phys.* **4** 516–20
- Baddour R E, Sherar M D, Hunt J W, Czarnota G J and Kolios M C 2005 High-frequency ultrasound scattering from microspheres and single cells *J. Acoust. Soc. Am.* **117** 934
- Beard P 2011 Biomedical photoacoustic imaging *Interface Focus* **1** 602–31
- Deihl D T 1968 'N waves' from bursting balloons *Am. J. Phys.* **36** 441
- Diebold G J, Khan M I and Park S M 1990 Photoacoustic 'signatures' of particulate matter: optical production of acoustic monopole radiation *Science* **250** 101–4
- Diebold G and Westervelt P 1988 The photoacoustic effect generated by a spherical droplet in a fluid *J. Acoust. Soc. Am.* **84** 2245
- Dukhin A S, Goetz P J and van de Ven T G M 2006 Ultrasonic characterization of proteins and blood cells *Colloids Surf. B: Biointerfaces* **53** 121–6
- Evans E and Fung Y-C 1972 Improved measurements of the erythrocyte geometry *Microvasc. Res.* **4** 335–47
- Godin M, Bryan A K, Burg T P, Babcock K and Manalis S R 2007 Measuring the mass, density, and size of particles and cells using a suspended microchannel resonator *Appl. Phys. Lett.* **91** 123121
- Gorelikov I, Martin A L, Seo M and Matsuura N 2011 Silica-coated quantum dots for optical evaluation of perfluorocarbon droplet interactions with cells *Langmuir* **27** 15024–33
- Gorelikov I and Matsuura N 2008 Single-step coating of mesoporous silica on cetyltrimethyl ammonium bromide-capped nanoparticles *Nano Lett.* **8** 369–73
- Grover W H, Bryan A K, Diez-Silva M, Suresh S, Higgins J M and Manalis S R 2011 Measuring single-cell density *Proc. Natl Acad. Sci.* **108** 10992–6
- Huynh E, Lovell J F, Helfield B L, Jeon M, Kim C, Goertz D E, Wilson B C and Zheng G 2012 Porphyrin shell microbubbles with intrinsic ultrasound and photoacoustic properties *J. Am. Chem. Soc.* **134** 16464–7
- Jensen J A 1996 FIELD: a program for simulating ultrasound systems *10th Nordicbaltic Conf. on Biomedical Imaging* vol 4 pp 351–3
- Jensen J A and Svendsen N B 1992 Calculation of pressure fields from arbitrarily shaped, apodized, and excited ultrasound transducers *IEEE Trans. Ultrason. Ferroelectr. Freq. Control* **39** 262–7
- Jongsma F H 1979 Liquids with a very low ultrasound propagation velocity *Ultrasonics* **17** 233
- Kim J-W, Galanzha E I, Shashkov E V, Moon H-M and Zharov V P 2009 Golden carbon nanotubes as multimodal photoacoustic and photothermal high-contrast molecular agents *Nat. Nanotechnol.* **4** 688–94
- Kohl Y, Kaiser C, Bost W, Stracke F, Fournelle M, Wischke C, Thielecke H, Lendlein A, Kratz K and Lemor R 2011 Preparation and biological evaluation of multifunctional PLGA-nanoparticles designed for photoacoustic imaging *Nanomed.: Nanotechnol. Biol. Med.* **7** 228–37

- Kolkman R G M, Hondebrink E, Steenbergen W and de Mul F F M 2003 *In vivo* photoacoustic imaging of blood vessels using an extreme-narrow aperture sensor *IEEE J. Sel. Top. Quantum Electron.* **9** 343–6
- Kripfgans O D, Fowlkes J B, Miller D L, Eldevik O P and Carson P L 2000 Acoustic droplet vaporization for therapeutic and diagnostic applications *Ultrasound Med. Biol.* **26** 1177–89
- Lovell J F, Jin C S, Huynh E, Jin H, Kim C, Rubinstein J L, Chan W C W, Cao W, Wang L V and Zheng G 2011 Porphysome nanovesicles generated by porphyrin bilayers for use as multimodal biophotonic contrast agents *Nat. Mater.* **10** 324–32
- Manohar S, Vaartjes S E, van Hespren J C G, Klaase J M, van den Engh F M, Steenbergen W and van Leeuwen T G 2007 Initial results of *in vivo* non-invasive cancer imaging in the human breast using near-infrared photoacoustics *Opt. Express* **15** 12277–85
- Marsh J N, Hall C S, Wickline S A and Lanza G M 2002 Temperature dependence of acoustic impedance for specific fluorocarbon liquids *J. Acoust. Soc. Am.* **112** 2858–62
- Matsuura N, Gorelikov I, Williams R, Wan K, Zhu S, Booth J, Burns P, Hynynen K and Rowlands J A 2009 Nanoparticle-tagged perfluorocarbon droplets for medical imaging *Materials Research Society Symp. Proc.* vol 1140
- Mohamed E T A, Kamanyi A E, Pluta M and Grill W 2012 Age-dependent acoustic and microelastic properties of red blood cells determined by vector contrast acoustic microscopy *Microsc. Microanal.* **18** 436–44
- Morse P M and Ingard K U 1968 *Theoretical Acoustics* (New York: McGraw-Hill)
- Narayana K L and Swamy K M 1989 Ultrasonic velocity in and adiabatic compressibility for some fluorocarbon liquid mixtures *J. Chem. Eng. Data* **34** 19–21
- Nasiriavanaki M, Xia J, Wan H, Bauer A Q, Culver J P and Wang L V 2013 High-resolution photoacoustic tomography of resting-state functional connectivity in the mouse brain *PNAS* **111** 11868
- Parker N G, Mather M L, Morgan S P and Povey M J W 2010 Longitudinal acoustic properties of poly(lactic acid) and poly(lactic-co-glycolic acid) *Biomed. Mater.* **5** 055004
- Saha R K and Kolios M C 2011 Effects of erythrocyte oxygenation on optoacoustic signals *J. Biomed. Opt.* **16** 115003
- Strohm E M, Berndl E S L and Kolios M C 2013a High frequency label-free photoacoustic microscopy of single cells *Photoacoustics* **1** 49–53
- Strohm E M, Elizabeth S L Berndl and Kolios M C 2013b Probing red blood cell morphology using high frequency photoacoustics *Biophys. J.* **105** 59–67
- Strohm E M, Gorelikov I, Matsuura N and Kolios M C 2012 Acoustic and photoacoustic characterization of micron-sized perfluorocarbon emulsions *J. Biomed. Opt.* **17** 096016–1
- Strohm E M and Kolios M C 2011 Sound velocity and attenuation measurements of perfluorocarbon liquids using photoacoustic methods *IEEE Int. Ultrasonics Symp. (Orlando, FL)* pp 2368–71
- Strohm E M, Rui M, Gorelikov I, Matsuura N and Kolios M 2011 Vaporization of perfluorocarbon droplets using optical irradiation *Biomed. Opt. Express* **2** 1432–42
- Strohm E M, Rui M, Kolios M C, Gorelikov I and Matsuura N 2010 Optical droplet vaporization (ODV): photoacoustic characterization of perfluorocarbon droplets *IEEE Int. Ultrasonics Symp.* pp 495–8
- Sun Y, Niu C, Wang Y, Strohm E M, Ran H, Zheng Y, Wang Z and Kolios M C 2013 Vaporization, photoacoustic and acoustic characterization of PLGA/PFH particles loaded with optically absorbing materials *IEEE Int. Ultrasonics Symp. (Prague, Czech Republic)* pp 132–5
- Treeby B E and Cox B T 2010 *k-Wave: MATLAB toolbox for the simulation and reconstruction of photoacoustic wave fields* *J. Biomed. Opt.* **15** 021314
- Tsytarev V, Rao B, Maslov K I, Li L and Wang L V 2013 Photoacoustic and optical coherence tomography of epilepsy with high temporal and spatial resolution and dual optical contrasts *J. Neurosci. Methods* **216** 142–5
- Volodkin D V, Skirtach A G and Möhwald H 2009 Near-IR remote release from assemblies of liposomes and nanoparticles *Angew. Chem. Int. Ed.* **48** 1807–9
- Wang L V 2009 *Photoacoustic Imaging and Spectroscopy* (Boca Raton, FL: CRC)
- Wang Z, Ha S and Kim K 2012 Evaluation of finite-element-based simulation model of photoacoustics in biological tissues *Proc. SPIE* **8320** 83201L
- Wang L V and Hu S 2012 Photoacoustic tomography: *in vivo* imaging from organelles to organs *Science* **335** 1458–62
- Wang X, Pang Y, Ku G, Xie X, Stoica G and Wang L V 2003 Noninvasive laser-induced photoacoustic tomography for structural and functional *in vivo* imaging of the brain *Nat. Biotechnol.* **21** 803–6

- Wang Y J, Strohm E M, Sun Y, Niu C, Zheng Y, Wang Z and Kolios M C 2014 PLGA/PFC particles loaded with gold nanoparticles as dual contrast agents for photoacoustic and ultrasound imaging *Proc. SPIE* **8943** 89433M
- Wilson K, Homan K and Emelianov S 2012 Biomedical photoacoustics beyond thermal expansion using triggered nanodroplet vaporization for contrast-enhanced imaging *Nat. Commun.* **3** 618
- Wintrobe M M, Greer J P and Lee G R 2009 *Wintrobe's Clinical Hematology* (Philadelphia, PA: Wolters Kluwer/Lippincott Williams & Wilkins)
- Xu B 2004 Numerical simulation of laser-generated ultrasound by the finite element method *J. Appl. Phys.* **95** 2116
- Xu B, Shen Z, Wang J, Ni X, Guan J and Lu J 2006 Thermoelastic finite element modeling of laser generation ultrasound *J. Appl. Phys.* **99** 033508
- Yao L and Jiang H 2009 Finite-element-based photoacoustic tomography in time domain *J. Opt. A: Pure Appl. Opt.* **11** 085301
- Yao J, Xia J, Maslov K I, Nasirivanaki M, Tsytsarev V, Demchenko A V and Wang L V 2013 Noninvasive photoacoustic computed tomography of mouse brain metabolism *in vivo NeuroImage* **64** 257–66
- Yi D K, Selvan S T, Lee S S, Papaefthymiou G C, Kundaliya D and Ying J Y 2005 Silica-coated nanocomposites of magnetic nanoparticles and quantum dots *J. Am. Chem. Soc.* **127** 4990–1
- Yuan Z and Jiang H 2007 3D finite-element-based photoacoustic tomography: reconstruction algorithm and simulations *Med. Phys.* **34** 538
- Zell K, Sperl J I, Vogel M W, Niessner R and Haisch C 2007 Acoustical properties of selected tissue phantom materials for ultrasound imaging *Phys. Med. Biol.* **52** N475–84
- Zhang H F, Maslov K, Stoica G and Wang L V 2006 Functional photoacoustic microscopy for high-resolution and noninvasive *in vivo* imaging *Nat. Biotechnol.* **24** 848–51